DOI: 10.1002/ ((please add manuscript number))

**Article type: Full Paper** 

Transparent, Flexible, Penetrating Microelectrode Arrays with Capabilities of

**Single-Unit Electrophysiology** 

Kyung Jin Seo, Pietro Artoni, Yi Qiang, Yiding Zhong, Xun Han, Zhan Shi, Wenhao Yao,

Michela Fagiolini\* and Hui Fang\*

K. J. Seo, Y. Qiang, Y. Zhong, Dr. X. Han, Z. Shi, W. Yao, Prof. H. Fang

Department of Electrical and Computer Engineering, Northeastern University, Boston,

Massachusetts 02115, USA

Dr. P. Artoni, Prof. M. Fagiolini

Center for Life Science, Boston Children's Hospital, Boston, Massachusetts 02115, USA

E-mail: Michela.Fagiolini@childrens.harvard.edu

Prof. H. Fang

Department of Bioengineering, Northeastern University, Boston, Massachusetts 02115, USA

Department of Mechanical and Industrial Engineering, Northeastern University, Boston,

Massachusetts 02115, USA

E-mail: h.fang@northeastern.edu

Keywords: transparent, flexible, penetrating, microelectrode array, spikes

1

#### **ABSTRACT**

Accurately mapping neuronal activity across brain networks is critical to understand behaviors, yet it is very challenging due to the need of tools with both high spatial and temporal resolutions. Here, we present penetrating arrays of flexible microelectrodes made of low-impedance nanomeshes which are capable of recording single-unit electrophysiological neuronal activity and at the same time, transparent, allowing to bridge electrical and optical brain mapping modalities. These 32-channel transparent penetrating electrodes with site area, 225  $\mu$ m², have a low impedance of ~ 149 k $\Omega$  at 1 kHz, an adequate charge injection limit of ~ 0.76 mC cm², and up to 100% yield. Mechanical bending tests reveal that the array is robust up to 1,000 bending cycles, and its high transmittance of 67% at 550 nm make them suitable for combining with various optical methods. A temporary stiffening using polyethylene glycol allowed the penetrating nanomesh arrays to be inserted into the brain minimally invasively, with *in vivo* validation of recordings of spontaneous and evoked single-unit activity of neurons across layers of the mouse visual cortex. Together these results establish a novel neurotechnology - transparent, flexible, penetrating microelectrode arrays - which possess great potential for brain research.

#### 1. Introduction

Technological advances in recording of neuronal activity from the brain have significantly spurred the development of neuroscience. Specifically, mapping activities of neuronal spikes (i.e., single-unit action potentials) is critical in decoding the function of neural circuits and understanding the dynamics of neural networks underpinning behavior. Detection and activation of single neurons of specific types would allow us to understand how neurons interact with each other in complex neural networks.<sup>[1]</sup> Evolved from the original single patch-clamp and wire, penetrating microelectrode arrays (MEAs) have established as the widely deployed devices to record and interpret neuronal spikes. Over the past few decades, various penetrating MEAs have been developed and deployed, such as industry-standard Utah and Michigan arrays. [2, 3] While these rigid conventional probes are adequate for acute studies, their performance typically degrades over repeated use. This degradation is mainly due to a large mechanical mismatch at the interface of these rigid electrodes and soft brain tissues.<sup>[4]</sup> To reduce the stress at the electrode/tissue interface, softer devices have been developed using flexible or stretchable polymers.<sup>[5-17]</sup> Since their Young's moduli are closer to those of the brain tissue, the mechanical mismatch is significantly lowered due to better mechanical compliance with tissue micromovements, brain expansion, and along with lower stress amplitude. Soft probes with polymer substrates comply more easily to supplicated biological topography, and their physical properties resemble those of neural tissue more closely, thus are less irritating to the biological environment.<sup>[18]</sup>

Another major limitation of MEA recording arises from the fact that pure electrical measurements, even from densely packed microelectrodes and probes, lack the inherent spatial resolution needed to differentiate cell type, shape and connections, which are all critical information to decipher the network activity of the brain. Recent advances in optical brain imaging and optogenetic interventions have produced enabling toolsets to target specific neuron types and resolve neuronal connections. As a result, there has been growing interests in

combining MEA recordings with optical approaches to leverage both the temporal and spatial resolution advantages from each method. Indeed, several past efforts, including our own work, have produced transparent MEAs from different materials to achieve the effective bridging of electrical and optical methods.<sup>[19-25]</sup> Transparent, penetrating MEAs can be used in various imaging techniques involving different imaging depths. Also, they are particularly advantageous when utilized in optogenetic experiments because their transparency will increase the light efficiency and less heat dissipation, preventing underlying tissue damage.<sup>[23]</sup> For future large-throughput penetrating MEAs, light access will become very difficult if the arrays are not transparent. However, there haven't been demonstrations of single-unit recording from existing transparent flexible MEAs, largely due to their high impedance. Consequently, there haven't been establishments of transparent flexible penetrating MEAs.

In this paper, we demonstrate the first transparent and flexible penetrating MEA, along with its validation of measuring single-unit recording *in vivo*. By miniaturizing microelectrodes made of gold (Au), poly(3,4-ethylenedioxythiophene)-poly(styrenesulfonate) (PEDOT:PSS) bilayer nanomesh, the microelectrodes achieved impedance of  $\sim 149~\rm k\Omega$  at 1 kHz at a  $15\times15~\rm \mu m^2$  site area (comparable to the size of a single neuron) while possessing 64% transparency at 550 nm, due to the functional nanomesh structure. The 32-ch penetrating nanomesh MEA has four tapered shanks. With a 30° tip angle, each of the shank is 1.4 mm long, 20  $\rm \mu m$  thick and 90  $\rm \mu m$  wide at its widest point. Systematic bench-top device characterizations demonstrated high yield, low impedance, high uniformity and great mechanical robustness, with bending reliability up to 1,000 cycles at a 4-mm bending radius. Nanomesh MEAs temporarily-stiffened by Polyethylene glycol (PEG) demonstrated well-behaved insertion dynamics in artificial brain phantoms and were inserted in the visual cortex of anesthetized mice using a similar stiffening approach. Significantly, we demonstrated successful *in vivo* insertion of the penetrating nanomesh MEAs with high-fidelity recordings of single-unit activities from different cortical layers in the brain, with efficient spontaneous and

visual-evoked spike detection across the 32 channels. The results here establish a promising type of transparent flexible penetrating MEAs, with broad applicability in both neuroscience and clinical applications.

#### 2. Results

#### 2.1. Flexible Penetrating Nanomesh MEAs

We fabricated the 32-channel transparent flexible penetrating MEAs using Au/PEDOT:PSS bilayer nanomeshes on Parylene C substrates (Figure S1). The device schematic shows four different layers stacked together to form a penetrating nanomesh MEA (Figure 1a). Specifically, a 15-µm-thick Parylene C layer served as a flexible and transparent substrate for the device. A nanomeshed bilayer of Au (25-nm-thick), PEDOT:PSS (105-nmthick) formed the electrode (225-µm<sup>2</sup> site area) and interconnect (7-µm line width, 3-µm gap between lines), providing excellent electrical conductivity and faradaic interface for low impedance and high recording signal-to-noise ratio (SNR). A final 4-um-thick SU-8 layer encapsulated the device and defined the 15×15 µm<sup>2</sup> windows, resulting in record-small transparent microelectrodes with a 100-µm pitch. Conventional transparent electrodes, such as indium tin oxide (ITO) and graphene, are highly transparent, but their electrochemical impedance is not low enough to allow scaling to the single-neuron size; when the impedance increases too high, the recording will suffer from increased thermal noise. The optical image of the device shows its transparency and structure, where the inset image, taken from an optical microscope, reveals further details of the shank and MEA profile (Figure 1b). Each shank has 8 channels and a length of 1.4 mm where the distance from the tip and the furthest channel is 800 µm, while there is also a reference electrode located on the two side shanks, adding up to 32 channels with 2 additional reference electrodes. The shanks have tapered profile with a tip angle of 30° to facilitate insertion and minimize tissue damage. [26] At the widest point, each shank has a cross-sectional footprint of 20×90 µm<sup>2</sup>. Scanning Electron Microscopy (SEM)

images show further details of all shanks and microelectrodes, also displaying the  $15\times15~\mu\text{m}^2$  electrode opening and the Au/PEDOT:PSS bilayer nanomesh structure (Figure 1c,d). The slight bending of the shanks demonstrates the mechanical flexibility of the device.

Figure 1e shows the fabrication process of the penetrating nanomesh MEA. Briefly, we first created bilayer nanomeshes of Au/PEDOT:PSS on a Parylene C film on a handling glass substrate using nanosphere lithography and template electroplating. Then, an e-beam evaporator deposited Ni to serve as a sacrificial layer to pattern the electrodes and interconnects. This Ni layer is critical in this step in order to achieve miniaturized electrodes and interconnects, due to the known poor adhesion of photoresists on PEDOT:PSS. After patterning bilayer nanomeshes using photolithography and ion milling, SU-8 encapsulation defined the electrode openings. By using another Ni as a hard mask, reactive ion etching (RIE) completely etched the non-protected Parylene C substrate and achieved the MEA profile including four shanks. Finally, carefully peeling off the device from the glass substrate completed the fabrication. Detailed fabrication process and parameters are explained in Experimental section.

#### 2.2. MEA Insertion Test

One of the main challenges of flexible shank MEAs arises from the insertion process where the most polymer-based devices could suffer from buckling, breaking or drifting away from the desired implant sites. Due to the biocompatibility requirement, the insertion footprint of the shanks need to be small, because otherwise there would be severe insertion trauma, tissue damage and resulted long-term tissue response. Reducing the dimension (both thickness and width) of the shank will have better compliance with the surrounding tissues. However, the shanks must also be rigid enough to insert into the soft tissue during implantation. Several solutions have arisen to facilitate the insertion process by using either rigid microneedles as shuttles, [6, 27, 28] or bio-dissolvable polymer coatings for temporary stiffening of the shanks. Among them, the bio-dissolvable coating approach appears to be more scalable to multiple

shanks and can easily prevent them from buckling during insertion all at once. Once inserted, these coatings can also slowly dissolve inside the brain within a few minutes. We therefore adopted this approach in this study. A few widely used coatings include silk, [29] maltose, [30] saccharose [31] and polyethylene glycol (PEG). [32, 33] We incorporated PEG here to stiffen our shanks over the other stiffening materials due to its prompt dissolving time and high Young's modulus, both of which are also controllable by different molecular weights. While there are various ways to coat PEG, such as dip-coating, we utilized a PDMS mold approach for PEG coating for its coating uniformality. [32] The groove depth in the PDMS mold was 100  $\mu$ m, yielding the total thickness of the PEG coating to be  $\sim 80 \mu$ m, which has been shown to make soft shanks hard enough to penetrate into the gel without any buckling, while allowing small insertion footprints (**Figure S2**).

We performed insertion of the nanomesh MEA shanks using 0.6% agarose gel brain phantoms to study their insertion mechanism. PEG coating stiffened the shanks and the interconnect parts to prevent buckling or even breaking during insertion. Figure 2a-b show the sequential steps involved in the insertion process in agarose gel at an insertion speed of 500  $\mu$ m/min, with measured force dynamics using a force gauge. We chose this insertion speed to minimize pressure and tissue damage, as evidently observed from previous *in vivo* experiments.<sup>[34]</sup> Indeed, the shanks with PEG coating can insert into the gel without any visual buckling. Once the tips touched the surface of the gel, the force started to increase. Right before the actual insertion, slight dimpling of the gel occurred until the probes had enough force to penetrate. At the time when the insertion happened, the force dropped slightly, then increased again when it penetrated further into the gel, consistent with previous studies. [18, 26] From our experiments, the first peak force (at step 3) was  $\sim$  0.8 mN for four shanks, indicating at least a 0.2 mN force is required for each shank to penetrate into the gel. Other studies of flexible penetrating electrodes also demonstrated insertion forces on the same order. [32, 35, 36] Compared to rigid shanks made of silicon or metals where the force during dimpling peaks much higher, [37]

flexible shanks have much lower forces during dimpling. This force of course varies from shanks to shanks depending on their tip angles, dimensions and insertion speed. Blunt tips, thick and wide shanks, and high insertion speed are the main factors that increase the insertion force, which could cause more damage to the brain. Also, having sharp tips with lower speed will minimize the dimpling of the tissue. [26, 38] The force kept rising after initial insertion due to increasing friction between the gel and the shank, and stopped when the insertion ceased. The maximum force of the insertion was 3.6 mN, at the time when the shanks were fully inserted. With the shanks stopped inside the gel, the force decreased and saturated to ~1.8 mN as time.

After full insertion, phosphate buffered saline (PBS) solution dissolved the PEG coating (step 6), demonstrating successful removal of the coating within a few minutes. The dissolving time varied based on the thickness of the coating. A high-definition video recording shows all these six steps with footprints (Movie S1). The microscope image of the four shanks inside the agarose gel appears in Figure 2c. All shanks and electrodes successfully resided in the gel without any buckling or other deformations, validating the effectiveness of this approach. We note that bare shank itself, without any kind of stiffening, could also penetrate into the gel with certain probability, but it tended to buckle inside the gel, likely due to continuous friction caused by the shank insertion, which made the microelectrodes to deviate from the desired destination and could also cause unwanted tissue damage during in vivo experiments. We further studied the retraction of the shanks with the same speed as we used for insertion (Figure S3). During retraction, the force decreased much quickly compared to insertion, eventually saturating at around zero. Other works also showed similar behaviors where the retraction force damped at a more rapid pace. [26, 35] Unlike silicon probes where they have relatively large dimpling force and big force drop upon insertion, [31] our flexible probes showed much smaller force and only a little drop at  $\sim 80$  sec (Figure S3). These differences presumably arise from the de-stiffening (dissolution) of PEG coating during the insertion, where our probe becomes softer as the insertion proceeds.

Theoretical analysis can shed light into the fundamental insertion process of the flexible nanomesh MEA shanks. From bending mechanics perspective, buckling force is the maximum force that a shank can withstand before bending and is defined by Euler's formula:<sup>[39]</sup>

$$F_{buckling} = \frac{\pi^2 I_{\chi E}}{(KL)^2} \tag{1}$$

$$I_{\mathcal{X}} = \frac{wt^3}{12} \tag{2}$$

where E is Young's modulus, K is column effective length factor, I is the area moment of inertia, L, w and t are length, width and thickness of the shank, respectively. By using this equation, we assume the shanks are beams fixed at one side (K=0.7) with constant cross-sectional area, not taking account the tapered profile. Assuming the E for Parylene C and PEG are 3.13 GPa<sup>[35]</sup> and 200 MPa,<sup>[32]</sup> respectively, calculation using the above formula yields buckling forces of 1.9 mN and 9.82 mN for without and with PEG coating, respectively. Since the required force for the brain penetration is on the order of  $\sim 1$  mN,<sup>[40]</sup> if the buckling force is on the same order as this force, there is high probability for the shanks to buckle and fail to penetrate, which is not reliable during the insertion. On the other hand, if the buckling force is one or a few orders of magnitude higher, the shanks will be highly likely to penetrate into the brain without buckling. The theoretical mechanical analysis here therefore explains our benchtop insertion studies and also provides simple guidelines for coating the PEG layer.

### 2.3. MEA Bench Testing

We performed bench testing of 32-channel penetrating nanomesh MEAs by immersing the devices in a PBS solution. The electrochemical impedance spectroscopy (EIS) response shows the electrochemical performance of a typical transparent microelectrode in the MEA with frequency ranging from 0.1 Hz to 1 MHz (**Figure 3**a). More insights on the electrochemical properties of the microelectrodes are revealed from the circuit model on the impedance and phase spectrum (**Figure S4**). The model consists a Warburg element ( $Z_W$ ) in

parallel with phase element  $(C_{PE})$ , which is then connected with pore resistance  $(R_P)$  in series. Together these three elements are in parallel with a coating capacitance ( $C_C$ ), then connected with solution resistance  $(R_S)$  in series. Compared to previous electrodes with the similar model,  $R_{\rm S}$  and  $C_{\rm C}$  values for our nanomesh electrode are significantly lower and higher, respectively.<sup>[41]</sup> This difference might be due to thicker PEDOT:PSS coating and the its side walls from the nanomesh structure. Encouragingly, the MEAs demonstrated up to 100% yield even at the aggressive design in this work. The histogram of the impedance at 1 kHz from all 32 microelectrodes show excellent uniformity, with an average impedance of  $149 \pm 32.5 \text{ k}\Omega$ (Figure 3b, S5). The spatial distribution of the electrode impedance with respect to their positions further illustrates the good uniformity of the array. The impedance of 149 k $\Omega$  at 1 kHz is not particularly low, but can be used to successfully detect spikes from the brain. It is possible to further decrease the impedance by deposition of more low-impedance coating while reducing some transparency of the device. To reveal the high-fidelity signal recording of the shanks, we performed bench-top recording using sine wave signals of 316  $\mu$ V<sub>pp</sub> at 1,000 Hz conducted into the PBS medium. Figure 3c, d show the recorded sine wave waveform and its power spectra density (PSD), respectively, after standard signal processing using a 0.1 ~ 5,000 Hz bandpass filter and notch filters to remove the 60 Hz (power line frequency) noise and its harmonics. The histogram of the noise distribution in all 32 channels also shows high signal-to-noise ratios (SNRs) and great uniformity. The average SNR value is  $28.8 \pm 3.1$  dB, corresponding to a 2.62μV root-mean-square (RMS) noise, which highlights low noise properties of these nanomesh microelectrodes. The penetrating nanomesh MEA also demonstrates medium-high transmittance over a 300 ~ 1,100 nm optical window with 67% transparency at 550 nm (Figure 3f). Unlike other transparent materials, by stacking a low-impedance film on top of a metal layer in the same nanomesh form, all functionalities including high electrical conductivity, low electrochemical impedance, and high optical transparency could be achieved simultaneously. These artificial nanomeshes therefore enable transparent microelectrodes to be scalable down

to a single neuron, around  $10\sim20~\mu m$  in diameter, while possessing excellent impedance characteristics. We note that the transparency of the electrodes can be further improved through optimizing the nanomesh pattern.

The electrodes in the penetrating nanomesh MEAs are also highly suitable for brain stimulation. Figure 3g shows the voltage transient profile of the Au/PEDOT:PSS nanomesh microelectrodes under a cathodic first, charge balanced, biphasic current pulse at 3.5 µA  $(0.4 \text{ mC cm}^{-2})$  with duration  $\sim 0.5 \text{ ms}$ . The voltage transient profile remains nearly identical after 4 million stimulation cycles of 0.4 mC cm<sup>-2</sup> charge injection, demonstrating the great reliability of the electrodes. Charge injection limit (CIL) measurement was carried out for all individual 32 channels to reveal their maximum charge injection performance. The average CIL was  $0.76 \pm 0.11$  mC cm<sup>-2</sup> (Figure 3h). The CIL of 0.76 mC cm<sup>-2</sup> is not particularly high, but provides suitable stimulation charges for various micro-stimulation applications on nerve tissue and retina prosthesis. [42, 43] Higher CIL for certain applications can also be achieved by further increasing the thickness of PEDOT:PSS while compromising little transparency. Lastly, mechanical robustness of the flexible penetrating MEAs is also crucial for device utilization and in vivo experiments. Our nanomesh MEAs demonstrated up to 1,000 cycles of bending with a radius of 4 mm (Figure 3i). During these bending cycles, we observed no significant performance degradation in impedance or yield, or any visual damages from the MEAs, highlighting their flexibility.

### 2.4. In vivo Validation

We then validated the *in vivo* recording capabilities of the transparent flexible penetrating MEAs in the mouse brain. After anesthetizing and positioning a juvenile mouse on a surgical stereotactic frame, about ~1 cm<sup>2</sup> of skin above the head was removed and both craniotomy and durotomy were performed on the visual cortex. **Figure 4**a shows the insertion of the PEG-coated shank arrays in the brain of the anesthetized mouse. The shanks were inserted

in the binocular portion of the primary visual cortex, at the stereotaxic coordinates of 2.8 mm lateral, 0.6 mm frontal from lambda. [44] The electrodes were successfully inserted with the same speed adopted for the phantom gel (500 µm/min). This procedure allowed no buckling of the electrodes during the insertion, consistent with what we witnessed from the *in vitro* insertion test. All the 8 electrodes in each shank were inserted, up to a total depth of 800 µm, allowing to probe the neuronal activity from the superficial layers down to layer V of the visual cortex. [45] The reference electrode of the MEA was intentionally left not inserted, since it was used to record electrical activity immediately from the saline solution added on top of the cortex, providing proper reference. The stereotaxic frame was connected to the common ground of the amplifier unit.

Spiking activity was detected on the majority of the electrodes (25 out of 32), 15 minutes after the insertion of the MEA, indicating that the PEG coating had sufficiently dissolved in the brain and that the tissue and neurons stabilized after the minimal stress arising from the insertion. All the electrodes were working, as shown by the similar fast Fourier transform (FFT) amplitude of their recordings (Figure S6). We measured both spontaneous and visual evoked single unit activity. The average waveforms of the spikes shown in Figure 4b are obtained by averaging spontaneous individual spike events in each channel (Figure 4c). The standard deviation of the amplitude among the spike population in one channel (reddish band in Figure 4c) indicates a stable *in vivo* recording. Moreover, despite the partial presence of PEG in the extracellular matrix might decrease the neuronal signal due to not complete metabolization during the recording, [46] the low impedance of the electrodes allowed reliable measurements, already recording 15 minutes after the insertion. We also tested the neuronal response to visual stimuli. In fact, some channels were found to be spiking more frequently during visual stimulation, indicating the activity of visually responsive cells (~1.5 fold during stimulation with moving gratings compared to isoluminous gray screen, Figure 4d, e). Finally, the MEA was removed from the brain at the end of the recording (Figure 4f), at the same speed

used for insertion. We didn't notice any visible damage in the electrodes after insertion and retraction, which in principle makes them suitable for PEG recoating and reusable multiple times. This data indicates that both the electrode design and the insertion method are compatible with *in vivo* recordings, with a noise low enough to detect spontaneous and evoked activity just a few minutes after the insertion.

#### 3. Conclusion

In summary, we successfully demonstrated transparent flexible penetrating MEAs from miniaturized Au/PEDOT:PSS bilayer nanomesh microelectrodes. Significantly, the results here proved that record-small, single-neuron-sized nanomesh microelectrodes were able to record single-unit activities in vivo, and that transparent flexible penetrating nanomesh MEAs were able to be inserted into the brain without jeopardizing the recording performance. Notably, the excellent electrode performance allows single-unit recording for the first time from transparent flexible electrodes. The low-impedance bilayer nanomesh microelectrodes here therefore also enabled the first transparent flexible penetrating MEAs with critical single-unit recording activity. Recordings in the mouse visual cortex have shown that the low-noise properties of the electrodes are sufficient to record both spontaneous and visual-evoked neuronal activity in mice, allowing them to be used in many acute and chronic *in vivo* electrophysiology experiments. We see no fundamental hurdles to demonstrate large-throughput, high-density nanomesh MEAs with close to or even more than one hundred channels for much more improved spatiotemporal resolution. In the future, these nanomesh microelectrodes are also applicable to various fields by simply tweaking their layout based on the region of the brain to probe. We envision that the high transparency of the MEAs makes them great candidates for coupling electrophysiology with various optical modalities, such as calcium imaging and optogenetics.

### 4. Experimental Section

Fabrication of bilayer nanomeshes on a Parylene C substrate: The fabrication began with the deposition of 15- $\mu$ m-thick Parylene C films with chemical vapor deposition on a silicon wafer using a SCS Parylene deposition system (PDS2010). Then, a Parylene C film was peeled off, flipped upside down and laminated onto a glass slide that was pre-spin-coated with 10:1 polydimethylsiloxane (PDMS, ~ 30  $\mu$ m). We note that the flipping is important to achieve high surface smoothness for further fabrication on the Parylene C film. An electron-beam (e-beam) evaporator then deposited Ti (2 nm)/SiO<sub>2</sub> (20 nm) as an etch stopper for the latter RIE step. To achieve the nanomeshes, we first scooped a layer of polystyrene spheres with an average size of 1  $\mu$ m in diameter using the air/water interface method. [47] RIE then trimmed the sizes of the spheres to ~ 950 nm to serve as a lift-off mask. Then, e-beam evaporator deposited Cr (3 nm)/Au (25 nm) where Cr acted as an adhesion layer between SiO<sub>2</sub> surface and Au layer. Lift-off in chloroform achieved Au nanomeshes with trace widths of ~ 100 nm. Finally, electrochemical deposition of PEDOT:PSS with current density of 0.2 mA/cm<sup>2</sup> and deposition time of 60 s on the Au nanomesh completed Au/PEDOT:PSS bilayer nanomesh fabrication on the Parylene C substrates.

Fabrication of 32-channel penetrating nanomesh MEAs: The fabrication began with e-beam evaporation of 30-nm-thick Ni on Au/PEDOT:PSS bilayer nanomeshes. We note that this Ni layer is needed to act as a sacrificial layer to pattern Au/PEDOT:PSS with small feature sizes due to that the adhesion between conventional photoresist (PR) and PEDOT:PSS was poor. After patterning the interconnects and electrodes with photolithography steps using PR S1805 (thickness of ~ 500 nm), ion milling for 15 mins (Veeco Microtech Ion Mill) etched Au/PEDOT:PSS/Ni layers altogether to achieve the device pattern, while with PR still on the samples as further protection. The etching parameters were 9 A of filament current, ~ 150 mA of beam current, 550 V of beam voltage, ~ 250 mA of emission current, 11 mA of accelerator current and 43 sccm of Ar. Due to the ion bombarding during ion milling, the PR became hard

to remove. Undercutting the underneath Ni using an iron (III) chloride (FeCl<sub>3</sub>) solution with gentle swabbing removed both Ni/PR layers at the same time. A 4  $\mu$ m-thick-SU-8 2005 then encapsulated and defined electrodes. We also defined the shank profile with SU-8 to minimize the etching time for latter profile etching. To define the MEA and shank profiles, e-beam evaporator deposited 300-nm-thick Ni as a hard mask. Photolithography with PR S1818 (thickness of  $\sim 1.8~\mu$ m) then formed the desire profile pattern. Inductively coupled plasma (ICP)-RIE (Unaxis Inductively coupled Plasma 790) etched the Parylene C substrate completely into shank profiles for 25 mins, in which the whole etching process was divided into four separate sessions to prevent heat accumulation of the samples. The etching parameters were 100 W for radio frequency 1 (RF<sub>1</sub>), 200 W for RF<sub>2</sub>, 25 mT for pressure, 18 sccm of O<sub>2</sub> and 2 sccm of CHF<sub>3</sub>.

Insertion experiment in brain phantoms: Before insertion, PEG (Alfa Aesar, molecular weight: 20,000 g/mol) coating stiffened the four shanks and their interconnect parts to prevent buckling or even breaking during the insertion. The PEG coating was performed using a pre-prepared PDMS mold, yielding a PEG thickness of 100  $\mu$ m, including the thickness of a shank. Then, the coated device was clamped with a grip and ensembled together to a motorized test stand (Mark-10 ESM303 Motorized Test Stand, Mark-10), equipped with a force gauge (Mark-10 M5-012, Mark-10). A 0.6% agarose gel (Agarose BP160-100, Fisher Scientific) was prepared to mimic the brain. We mixed the gel powder and deionized (DI) water, and stirred for a few hours at 140 °C until the solution became transparent. Then, the solution cooled down at room temperature which formed the gel. The shanks slowly moved down with a speed of 500  $\mu$ m/min into the agarose gel to study the insertion mechanism. The video was recorded with a camera (Canon EOS) equipped with three extension lenses (making up to  $\sim$  100 mm of focal length) for high-magnification.

*Mice*. Wild-type (WT) (C57BL/6J; JAX 000664) mice were purchased from Jackson Laboratories. All mice were raised from breeding pairs in our colony and housed with up to

four littermates under standard laboratory conditions (12:12-h inverted light:dark cycle; access to water and food ad libitum). Animal care and experimental procedures were performed in accordance with protocols approved by the Boston Children's Hospital Institutional Animal Care and Use Committee (IACUC).

In vivo electrophysiology and data analysis: The acute electrophysiology experiment consisted in a cranial window surgery followed by electrode implantation and recording. The mouse was anesthetized using isoflurane (induction 3%, maintain 1-1.5%), and then placed on a stereotaxic frame. After shaving and removing the skin on the skull, a small portion of the skull on the visual cortex was removed (3 mm wide circular craniotomy) using a dental drill. Then the dura was removed using forceps, and the electrode was inserted using a micromanipulator (IMS-10, Narishige), with the insertion speed of 500 µm/min. The surface of the brain was kept hydrated using saline. The internal temperature of the mouse was kept at 38 °C using a thermal pad. 15 minutes after the insertion of the electrodes, the activity of the visual cortex was recorded using alternating visual stimulation to iso-luminous gray stimuli (no visual stimulation, to record spontaneous activity). Data were recorded with a hardware band pass filter of 0.1 Hz 30 kHz. A digital bandpass filter was applied to the data for single unit analysis (performed in MATLAB) from 500 Hz to 5000 Hz. Custom written MATLAB scripts are available upon request. A digital bandpass filter from 0.1 Hz to 200 Hz and a notch filter at 60 Hz (for removing power-line frequency) were used for doing frequency analysis of the Local Field Potential (LFP) across the different electrodes.

Visual stimuli presentation: Visual stimuli were presented on a 6.5×11.5 cm<sup>2</sup> screen (60 Hz refresh), controlled by an arduino shield (Gameduino3, ExCamera labs). The gamma curve of the screen was calibrated with a photometer to achieve a linear response. A TTL signal was sent from the arduino to the digital input port of the acquisition board (Intan 128ch Stimulation/Recording Controller, Intantech) when the visual stimuli were presented. The screen was placed frontally, at 3 cm from the eyes of the mouse. Stimuli consisted in sinusoidal

moving gratings with temporal frequency of 2 Hz, and spatial frequency of 0.03 deg<sup>-1</sup>, 100% contrast. Stimuli were alternated with gray screen of the same luminance. Custom written code is available upon request.

Statistical Analysis: All data points for both bench testing and *in vivo* data have been calculated using MATLAB and are presented as mean ± standard deviation, using Origin 2018b software. Error bars and error bands within the size of the datapoints are not shown. Normal distributions have been fitted with a gaussian curve. For each statistical analysis, the experiments were repeated at least three times, unless otherwise noted. In the analysis of the *in vivo* data, spikes were averages across the spike population on each channel. In all experiments, p-values < 0.05 were considered significant. No data were rejected.

### **Supporting Information**

Supporting Information is available from the Wiley Online Library. SEM images of Au nanomesh; PEG coating characterization with SEM; Insertion profile with both insertion and retraction; Impedance circuit model with detailed equation and fitted values; Impedance histogram of different penetrating MEAs; Power spectrum of the 32-channel MEA during spontaneous activity (no visual stimulation); a video recording of shanks inserting into an agarose gel.

### Acknowledgements

K. J. S. and P. A. contributed equally to this work. This work was supported by Northeastern University, Samsung GRO program, NIH National Institute of Neurological Disorders and Stroke (R01NS095959), Rettsyndrome.org, Rett Syndrome Research Trust, Simon Foundation, Human Frontier Science Program—Cross-Disciplinary Fellowship, and World Premier International Research Initiative—International Research Center for Neurointelligence (Japan Society for the Promotion of Science) [WPI-IRCN (JSPS)]. We would like to thank the

cleanroom staff of George J. Kostas Nanoscale Technology and Manufacturing Research Center at Northeastern University for technical help.

Received: ((will be filled in by the editorial staff))

Revised: ((will be filled in by the editorial staff))

Published online: ((will be filled in by the editorial staff))

### References

- [1] Q. Bai, K. D. Wise, *IEEE Trans. Biomed. Eng.* **2001**, 48, 911.
- [2] E. M. Maynard, C. T. Nordhausen, R. A. Normann, *Electroencephalogr. Clin. Neurophysiol.* **1997**, *102*, 228.
- [3] A. C. Hoogerwerf, K. D. Wise, *IEEE Trans. Biomed. Eng.* **1994**, *41*, 1136.
- [4] A. Weltman, J. Yoo, E. Meng, *Micromachines* **2016**, *7*, 180.
- [5] V. Castagnola, E. Descamps, A. Lecestre, L. Dahan, J. Remaud, L. G. Nowak, C. Bergaud, *Biosens. Bioelectron.* **2015**, *67*, 450.
- [6] L. Luan, X. Wei, Z. Zhao, J. J. Siegel, O. Potnis, C. A. Tuppen, S. Lin, S. Kazmi, R. A. Fowler, S. Holloway, *Sci. Adv.* **2017**, *3*, e1601966.
- [7] S. Felix, K. Shah, D. George, V. Tolosa, A. Tooker, H. Sheth, T. Delima, S. Pannu, presented at *Conf. Proc. IEEE Eng. Med. Biol. Soc.*, **2012**.
- [8] F. Barz, P. Ruther, S. Takeuchi, O. Paul, presented at *Micro. Electro. Mech. Syst.* (MEMS), 2015 28th IEEE Int. Conf., 2015.
- [9] H.-Y. Lai, L.-D. Liao, C.-T. Lin, J.-H. Hsu, X. He, Y.-Y. Chen, J.-Y. Chang, H.-F. Chen,
   S. Tsang, Y.-Y. I. Shih, *J. Neural Eng.* 2012, 9, 036001.
- [10] P. R. Patel, K. Na, H. Zhang, T. D. Kozai, N. A. Kotov, E. Yoon, C. A. Chestek, *J. Neural. Eng.* **2015**, *12*, 046009.
- [11] A. W. Hirschberg, H. Xu, K. Scholien, T. W. Berger, D. Song, E. Meng, presented at *Micro. Electro. Mech. Syst. (MEMS)*, 2017 IEEE 30th Int. Conf., 2017.
- [12] T. G. Schuhmann Jr, J. Yao, G. Hong, T.-M. Fu, C. M. Lieber, *Nano Lett.* **2017**, *17*, 5836.
- [13] D. Khodagholy, J. N. Gelinas, G. Buzsáki, *Science* **2017**, *358*, 369.
- [14] D. Khodagholy, J. N. Gelinas, Z. Zhao, M. Yeh, M. Long, J. D. Greenlee, W. Doyle, O. Devinsky, G. Buzsáki, *Sci. Adv.* **2016**, *2*, e1601027.
- [15] J. M. Murbach, S. Currlin, A. Widener, Y. Tong, S. Chhatre, V. Subramanian, D. C.

- Martin, B. N. Johnson, K. J. Otto, MRS Commun. 2018, 8, 1043.
- [16] J. Pas, A. L. Rutz, P. P. Quilichini, A. Slézia, A. Ghestem, A. Kaszas, M. J. Donahue, V.
  F. Curto, R. P. O'Connor, C. Bernard, *J. Neural Eng.* 2018, 15, 065001.
- [17] A. Williamson, M. Ferro, P. Leleux, E. Ismailova, A. Kaszas, T. Doublet, P. Quilichini,
   J. Rivnay, B. Rózsa, G. Katona, *Adv. Mater.* 2015, 27, 4405.
- [18] A. Lecomte, E. Descamps, C. Bergaud, J. Neural Eng. 2018, 15, 031001.
- [19] D. W. Park, A. A. Schendel, S. Mikael, S. K. Brodnick, T. J. Richner, J. P. Ness, M. R. Hayat, F. Atry, S. T. Frye, R. Pashaie, S. Thongpang, Z. Ma, J. C. Williams, *Nat. Commun.* **2014**, *5*, 5258.
- [20] D. Kuzum, H. Takano, E. Shim, J. C. Reed, H. Juul, A. G. Richardson, J. de Vries, H. Bink, M. A. Dichter, T. H. Lucas, D. A. Coulter, E. Cubukcu, B. Litt, *Nat. Commun.* **2014**, *5*, 5259.
- [21] P. Ledochowitsch, E. Olivero, T. Blanche, M. M. Maharbiz, presented at *2011 Ann. Int. Conf. of the IEEE Eng. Med. Biol. Soc.* **2011**.
- [22] K. Y. Kwon, B. Sirowatka, W. Li, A. Weber, presented at 2012 IEEE Biomed. Circuits Syst. Conf. (BioCAS) 2012.
- [23] J. Lee, I. Ozden, Y.-K. Song, A. V. Nurmikko, *Nat. Methods* **2015**, *12*, 1157.
- [24] Y. Qiang, K. J. Seo, X. Zhao, P. Artoni, N. H. Golshan, S. Culaclii, P. M. Wang, W. Liu,K. S. Ziemer, M. Fagiolini, *Adv. Funct. Mater.* 2017, 27, 1704117.
- [25] Y. Qiang, P. Artoni, K. J. Seo, S. Culaclii, V. Hogan, X. Zhao, Y. Zhong, X. Han, P.-M. Wang, Y.-K. Lo, Y. Li, H. A. Patel, Y. Huang, A. Sambangi, J. S. V. Chu, W. Liu, M. Fagiolini, H. Fang, *Sci. Adv.* **2018**, *4*.
- [26] A. Andrei, M. Welkenhuysen, B. Nuttin, W. Eberle, J. Neural Eng. 2011, 9, 016005.
- [27] H. S. Sohal, A. Jackson, R. Jackson, G. J. Clowry, K. Vassilevski, A. O'Neill, S. N. Baker, *Front. Neuroeng.* **2014**, *7*, 10.
- [28] J. T. Kuo, B. J. Kim, S. A. Hara, C. D. Lee, C. A. Gutierrez, T. Q. Hoang, E. Meng, Lab.

- Chip. 2013, 13, 554.
- [29] F. Wu, L. Tien, F. Chen, D. Kaplan, J. Berke, E. Yoon, presented at *Solid-State Sens*. *Actuators and Microsyst. 2013 Transducers & Eurosensors XXVII: The 17th Int. Conf.* **2013**.
- [30] Z. Xiang, S.-C. Yen, N. Xue, T. Sun, W. M. Tsang, S. Zhang, L.-D. Liao, N. V. Thakor,C. Lee, J. Micromech. Microeng. 2014, 24, 065015.
- [31] C. Hassler, J. Guy, M. Nietzschmann, D. T. Plachta, J. F. Staiger, T. Stieglitz, *Biomed. Microdevices* **2016**, *18*, 81.
- [32] A. Lecomte, V. Castagnola, E. Descamps, L. Dahan, M. Blatché, T. Dinis, E. Leclerc,C. Egles, C. Bergaud, *J. Micromech. Microeng.* 2015, 25, 125003.
- [33] K. Bjugstad, D. Redmond Jr, K. Lampe, D. Kern, J. Sladek Jr, M. Mahoney, *Cell Transplant.* **2008**, *17*, 409.
- [34] A. A. Sharp, A. M. Ortega, D. Restrepo, D. Curran-Everett, K. Gall, *IEEE Trans. Biomed. Eng.* **2009**, *56*, 45.
- [35] A. Weltman, H. Xu, K. Scholten, T. Berger, E. Meng, presented at *Proc. Hilton Head Workshop*, **2016**.
- [36] B. J. Kim, C. A. Gutierrez, G. A. Gerhardt, E. Meng, presented at *Micro. Electro. Mech. Syst. (MEMS)*, 2012 IEEE 25th Int. Conf. 2012.
- [37] N. H. Hosseini, R. Hoffmann, S. Kisban, T. Stieglitz, O. Paul, P. Ruther, presented at Eng. Med. Biol. Soc. EMBS 2007. 29th Ann. Int. Conf. IEEE, 2007.
- [38] S. Singh, M.-C. Lo, V. B. Damodaran, H. M. Kaplan, J. Kohn, J. D. Zahn, D. I. Shreiber, *Sensors* **2016**, *16*, 330.
- [39] P. J. Rousche, D. S. Pellinen, D. P. Pivin, J. C. Williams, R. J. Vetter, D. R. Kipke, *IEEE Trans. Biomed. Eng.* **2001**, *48*, 361.
- [40] B. Wester, R. Lee, M. LaPlaca, J. Neural Eng. 2009, 6, 024002.
- [41] M. R. Abidian, D. C. Martin, *Biomaterials* **2008**, *29*, 1273.
- [42] S. F. Cogan, Annu. Rev. Biomed. Eng. 2008, 10, 275.

- [43] J. D. Weiland, W. Liu, M. S. Humayun, Annu. Rev. Biomed. Eng. 2005, 7, 361.
- [44] M. E. Garrett, I. Nauhaus, J. H. Marshel, E. M. Callaway, J. Neurosci. 2014, 34, 12587.
- [45] W. Ji, R. Gămănuţ, P. Bista, R. D. D'Souza, Q. Wang, A. Burkhalter, Neuron 2015, 87,

632.

- [46] K. Bjugstad, K. Lampe, D. Kern, M. Mahoney, *J. Biomed. Mater. Res. Part A* **2010**, *95*,79.
- [47] K. J. Seo, Y. Qiang, I. Bilgin, S. Kar, C. Vinegoni, R. Weissleder, H. Fang, *ACS nano* **2017**, *11*, 4365.

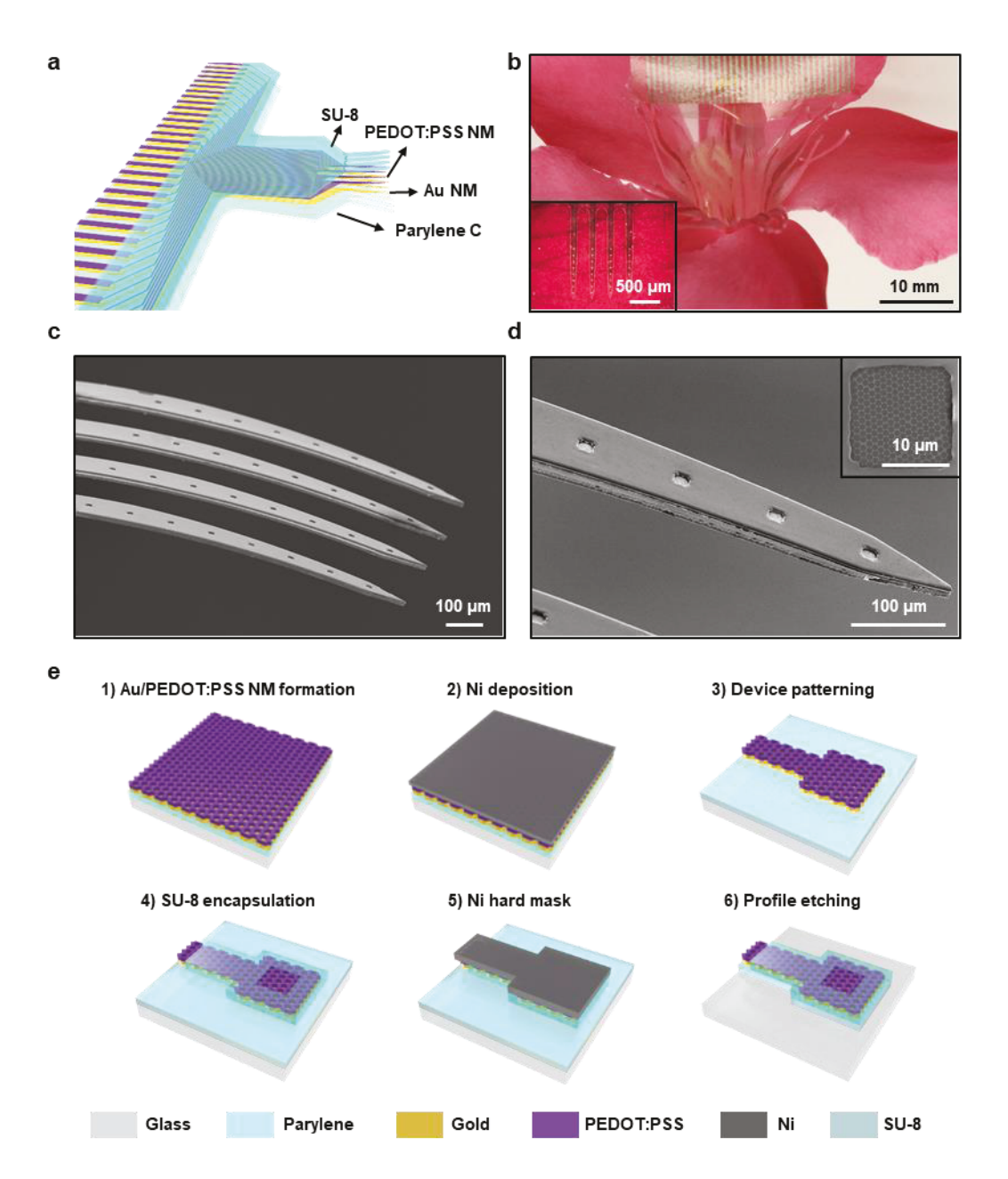


**Figure 1. Overview of the 32-channel transparent flexible penetrating MEA description and its fabrication.** a) Device schematic of the 32-channel Au/PEDOT:PSS bilayer nanomesh MEA. b) Optical image of the device in a pink azalea with an anisotropic conductive film (ACF) cable connected, inset: microscope image of four shanks on a flower petal. c) SEM image of four shanks. d) Zoomed-in SEM image of one individual shank, inset: SEM image of a single 15×15 μm²-sized electrode revealing the bilayer nanomesh. e) Fabrication process: 1. Bilayer nanomesh formation on a Parylene C substrate using lift-off and electrodeposition. (See

methods for details), 2. Ni deposition with e-beam evaporator, 3. Device patterning with conventional photolithography and ion milling, 4. SU-8 encapsulation, 5. Ni hard mask deposition with e-beam evaporator and pattern the profile accordingly, and 6. MEA profile etching with RIE.

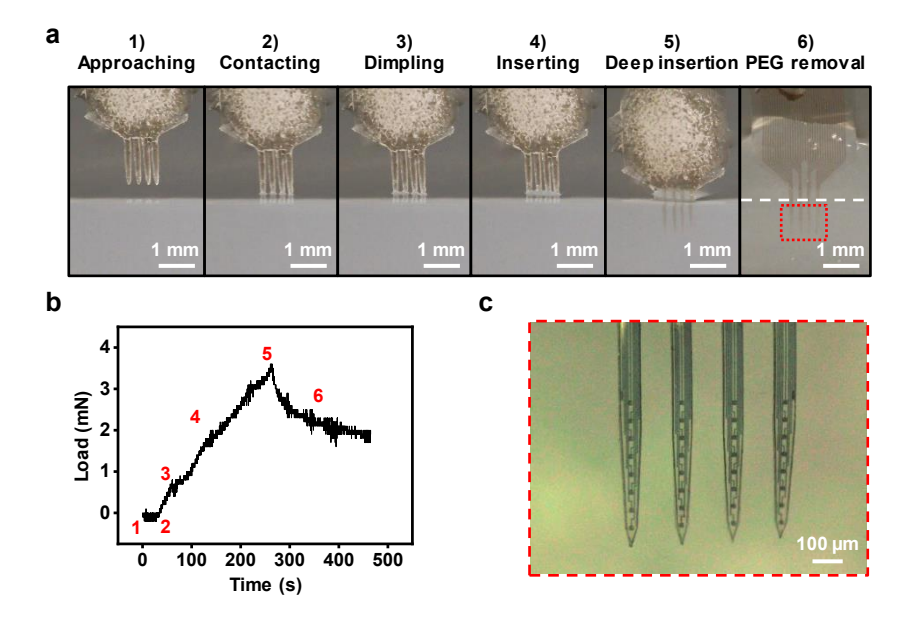


Figure 2. Insertion mechanism of the 32-channel transparent flexible penetrating MEA.

a) Series of optical images showing insertion of the shanks into a 0.6% agarose gel brain phantom with a speed of  $500 \, \mu m/min$ . b) Force profile of the device during the insertion process, with red numbers in correspondence with (a). c) Microscope image of four shanks resided in the gel phantom.

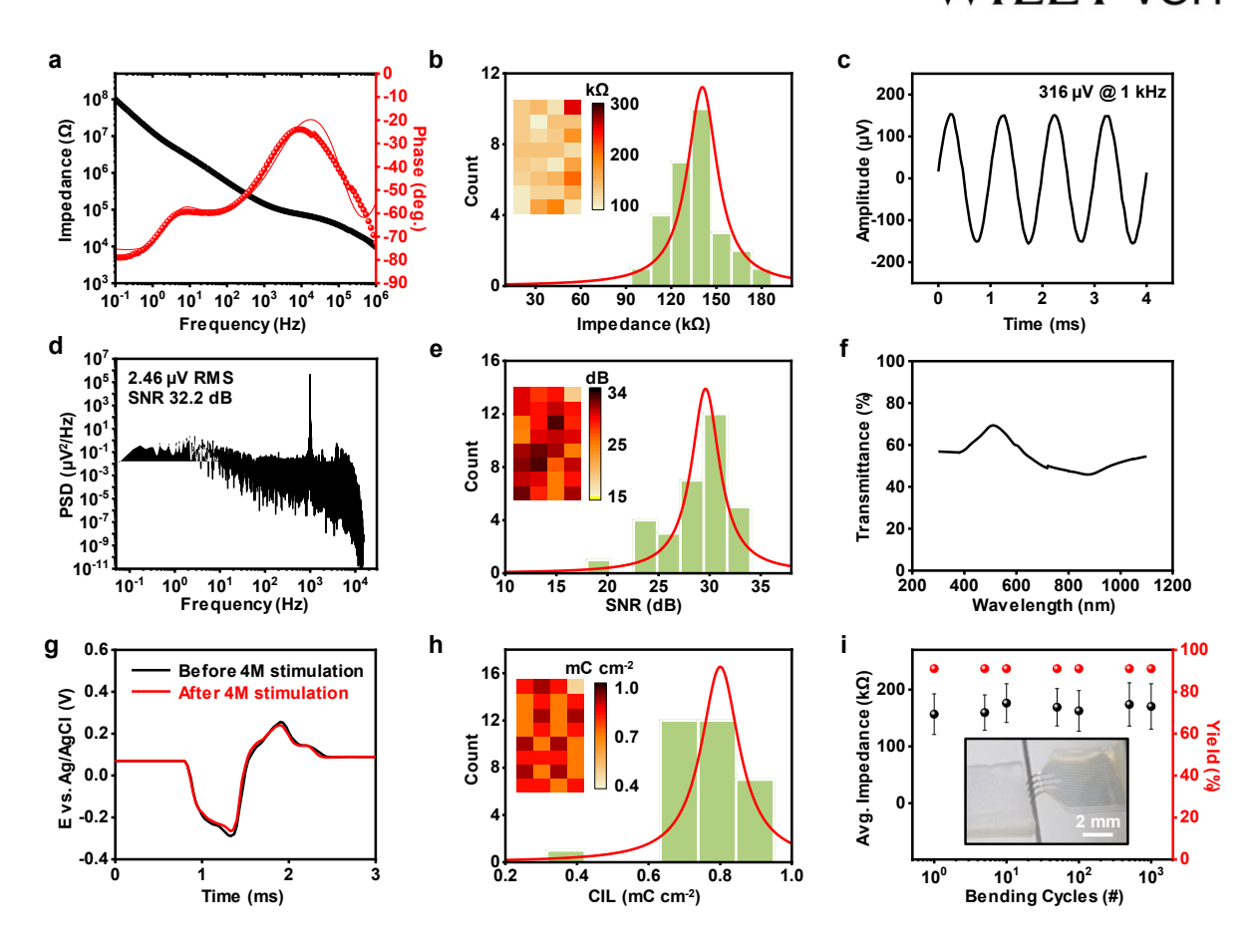


Figure 3. Bench characterizations of the 32-channel transparent flexible penetrating MEA.

a) Impedance magnitude and phase spectra of a representative channel in a 32-ch penetrating nanomesh MEA. b) Electrode-impedance histogram of the 32-ch penetrating MEA in (a), inset: impedance colormap with respect to actual channel position. c) Bench recording output of a 1,000 Hz, 316  $\mu$ V<sub>pp</sub> sine wave input using the penetrating MEA in (a). d) Power spectra density (PSD) of recorded sine wave output in (c). e) SNR histogram from all 32-ch electrodes with the bench recording in (c), inset: SNR colormap with respect to actual channel position. f) Transmittance spectrum of the penetrating nanomesh MEA. g) Voltage transient curve for the charge injection limit. h) CIL histogram from all 32-ch electrodes with bench recording in (f). i) Average electrode impedance and array yield as a function of bending cycles with a bending radius of 4 mm.

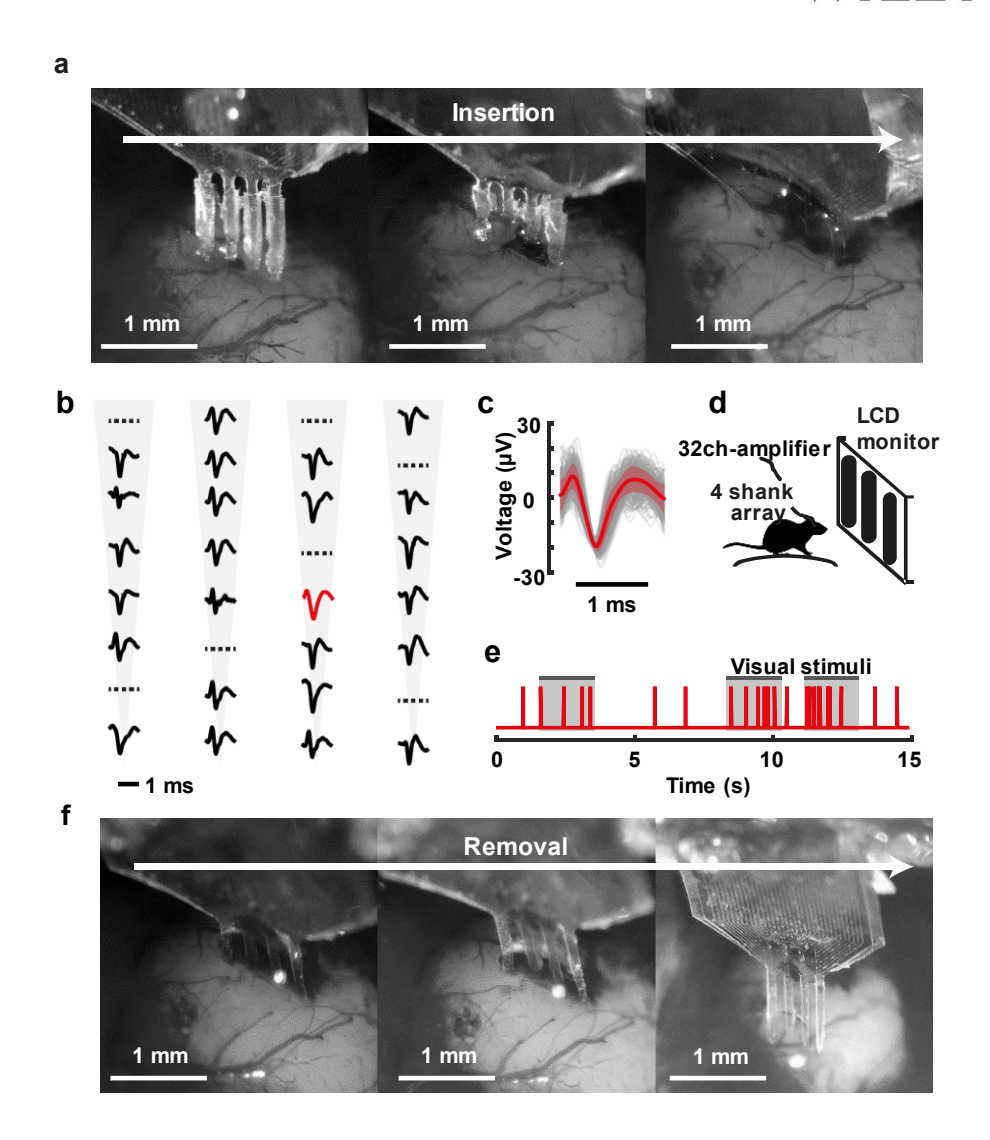


Figure 4. In vivo recording of spiking activity using the penetrating nanomesh MEA from the visual cortex of an anesthetized mouse. a) Insertion of the 32-ch penetrating MEA (4 shanks × 8 electrodes layout) in the visual cortex of an anesthetized mouse, using a micromanipulator. b) Average spontaneous spiking activity recorded from each channel of the MEA. Dashed dots indicate no spike detection. c) Single events recorded from one electrode (gray) and average of these events (red). Band indicates standard deviation. d) Artwork of visual stimulation (moving gratings). e) Single spiking events of a visually responsive cell triggered by visual stimuli. f) Removal of the electrodes from the cortex.

**Transparent microelectrodes are great candidates for combining electrophysiology with optical modalities.** Here, using advanced nanomesh technology, a transparent, flexible, penetrating microelectrode array is demonstrated with high yield, low impedance, high uniformity, and great mechanical robustness. Insertion and recording in a mouse visual cortex successfully validate this array *in vivo*, with detection of both spontaneous and evoked single-unit activity of neurons.

**Keyword:** transparent, flexible, penetrating, microelectrode array, spikes

Kyung Jin Seo, Pietro Artoni, Yi Qiang, Yiding Zhong, Xun Han, Zhan Shi, Wenhao Yao, Michela Fagiolini\* and Hui Fang\*

Transparent, Flexible, Penetrating Microelectrode Arrays with Capabilities of Single-Unit Electrophysiology

ToC figure

